Roll-to-roll compatible flexible polymer solar cells incorporating a water-based solution-processable silver back electrode with low annealing temperature

Giovanni Iannaccone [a], Marja Välimäki [b], Elina Jansson [b], Antti Sunnari [b], Gianni Corso [c], Andrea Bernardi [c], Marinella Levi [a], Stefano Turri [a], Jukka Hast [b], Gianmarco Griffini [a,*]

[a] *Department of Chemistry, Materials and Chemical Engineering "Giulio Natta", Politecnico di Milano, Piazza Leonardo da Vinci 32, 20133 Milano, Italy*
[b] *VTT Technical Research Centre of Finland, P.O. Box 1100 FI-90570, Oulu, Finland*
[c] *ENI S.p.A., Research Center for Renewable Energies and Environment-Istituto Donegani, Via Giacomo Fauser 4, 28100 Novara, Italy*

Received 8 May 2015
Received in revised form
24 June 2015
Accepted 27 June 2015
Available online 20 July 2015

1. Introduction

Polymer solar cells (PSCs) have attracted considerable attention in the last few decades because of their intrinsic lightweight, their potential transparency, the possibility to fabricate them on flexible substrates, and the low-cost production, the latter being potentially achievable by means of all solution and large-scale roll-to-roll (R2R) processing [1–4]. The research efforts of the PSC com-munity have been largely focused on the optimization of the performance of devices, which are typically based on a photoactive bulk heterojunction (BHJ) constituted by an electron-donating conjugated polymer and an electron-accepting fullerene derivative [5–9]. In a typical laboratory scale PSC stack the deposition of the photoactive blend is followed by the thermal evaporation of a low work-function metallic back electrode (typically aluminum) that works as cathode, in order to produce the so-called standard architecture. Optimization of this device geometry has allowed in the past few years a tremendous performance improvement and power conversion efficiencies (PCEs) exceeding 11% which have been recently demonstrated [10]. Despite its high efficiency, this device architecture presents some technological drawbacks. On one hand, it is characterized by a relatively low environmental stability, especially due to the thermal and photo-degradation of the BHJ and to oxidation reactions ascribed to the air-sensitive low work function electrode [11–15]. On the other hand, a vacuum processing step is still required for back-electrode deposition, the latter being directly incorporated on top of the photoactive layer thus limiting significantly the possibility to employ solution-based techniques for its deposition [16]. In particular, the vacuum evaporation step used for back-electrode fabrication in standard systems still represents a very crucial issue for the PSC technology as it strongly limits production speed of these devices, especially in

* Corresponding author. Tel.: +39 02 2399 3213.
E-mail address: gianmarco.griffini@polimi.it (G. Griffini).

view of the high throughput requirements typical of R2R-compatible processing techniques.

In order to overcome some of these limitations, the so-called inverted geometry has been introduced [17–19]. In this architecture, the polarity of the PSC device is modified by depositing a high work-function metal on top of the PSC stack that serves as hole-collecting electrode. As a result, the inverted geometry has allowed the use of solution-processable formulations for the deposition of the metal back-electrode. Indeed, in this case a hole-transporting layer (HTL) is interposed between the photoactive layer and the metallic electrode that acts as a buffer layer for electrons and helps to prevent chemical degradation of the underlying BHJ. To achieve fully solution-processable inverted PSC systems amenable for easy scale-up, a suitable silver formulation is commonly used as the precursor of the metallic back-electrode, which is deposited onto the HTL (most commonly poly(3,4-ethylenedioxythiophene):poly-(styrenesulfonate)-PEDOT:PSS) by means of printing and coating techniques compatible with R2R processing including flatbed and rotary screen printing [1,3,20], spray coating [21–23], inkjet printing [20,24,25] and flexographic printing [20]. The use of these R2R-compatible techniques has also been demonstrated for the processing of other PSC functional layers, including the photoactive element. However, in this case such high-speed R2R-compatible processing methods may not allow sufficient time for the formation of a favorable optimized BHJ morphology, thus the performance of the resulting devices is still found to be somewhat lower than spin-cast PSC devices followed by post-treatments [3,26,27].

The deposition of the silver back-electrode is challenging since it is performed during the final step of the PSC multilayer stack fabrication, thus the process entails some critical technological considerations. First of all, relatively low annealing temperatures are required in order to avoid morphological degradation of the underlying organic layers (especially the BHJ) and incompatibility with flexible plastic substrates such as polyethylene terephthalate (PET) [28]. Another important aspect is the undesired interaction between the solvent used in the silver ink formulation and the underlying photoactive BHJ material arising from potential ink diffusion through the buffer HTL that leads to poor device performance [24,25]. The ink formulations commonly used for the fabrication of the silver back-electrode are typically based on micro- or nano-sized metal particles, usually dispersed in an organic medium. Typical sintering temperatures in the 120–140 °C range are required in order to achieve high ink conductivity values [1,16,21,22]. Interestingly, recent life cycle analysis studies on PSCs have shown that lower annealing temperatures and the use of non-toxic solvents such as water in ink formulations for the metallic back-electrode may contribute to lower the production costs of these devices [29], making the PSC technology more attractive due to a potential further reduction of the cost per unit of produced electricity. In addition, the use of water-based metallic inks may lead to a lower environmental impact of the PSC tech-nology with respect to more common solvent-based approaches. Despite these potential advantages, no examples of the use of water-based particle-free ink formulations for the solution-based deposition of the silver back-electrode in inverted PSC devices at mild annealing temperatures have been presented in the literature to date.

Accordingly, in this work a water-based silver ink formulation was developed to be used as precursor for the fabrication of the metallic back-electrode in inverted flexible PSC devices. Such solution-processable particle-free reactive ink exploits the reduction of a diamminesilver (I) complex in aqueous medium to form a highly conductive film at mild annealing temperatures (90 °C), thus significantly limiting the morphological and thermal degra-dation of the underlying PSC layers and potentially lowering the costs of PSC fabrication. Functional tests were performed on flexible inverted PSC devices incorporating this silver-based reactive ink as the precursor for the metallic back-electrode entirely fabricated by means of R2R-compatible processes. In order to investigate the effect of the deposition of the reactive ink on the underlying PSC layers, different back-electrode architectures were investigated and thoroughly characterized. In addition, the influence of the thickness of the PEDOT:PSS HTL on the functional performance of the PSC devices was also investigated and an optimized combination of back-electrode architecture and PEDOT:PSS thickness was found, that also allowed to obtain semi-transparent PSC devices. To the best of our knowledge, this study represents the first demonstration of direct R2R-compatible printing deposition of a reactive water-based silver ink formulation as precursor for the back-electrode in flexible inverted PSCs devices.

2. Experimental

2.1. Reactive silver ink formulation

The reactive silver ink was synthesized based on previously published work [30]. Briefly, silver acetate was firstly dissolved in aqueous ammonium hydroxide in a 1:10 M ratio and formic acid was then added dropwise into the solution that was magnetically stirred. The ink was obtained from the clear supernatant separated by centrifugation from the silver particles formed during the addition of formic acid. The ink formulation was modified by adding a mixture of 2-propanol (IPA) and 1-ethoxy-2-propanol (EP) (EP:IPA = 7:3 w/w) as diluents and polyvinylpyrrolidone (PVP) K 90 (average M_w = 360,000 g/mol) as binder. The as-prepared modified reactive ink formulation was magnetically stirred for 3 h before printing to allow complete dissolution of all components. All reagents were purchased from Sigma-Aldrich unless otherwise stated.

2.2. PSCs fabrication

Indium–tin-oxide (ITO) coated PET substrates (40–60 Ω/sq, Eastman) were patterned using an etching paste (Isishape Hiper-Etch, Merck KGaA). The paste was R2R rotary screen-printed onto the ITO as an indirect image, thermally treated, and cleaned to remove the excess on the substrates. A 5 wt% solution of ZnO nanoparticles (Nanograde, Switzerland) dissolved in ethanol was gravure printed using a table-top gravure printer (Labratester, Norbert Schläfli Maschinen) [31,32].

The photoactive layer was gravure printed using a 131 mg/mL solution of poly-3-hexylthiophene (P3HT, Rieke Metals):[6. 6]-phenyl-C_{61}-butyric acid methyl ester (PCBM, Nano-C) in 1,2-dichlorobenzene (Sigma-Aldrich). The P3HT:PCBM ratio was 1:0.62 by weight. After gravure printing, the film was immediately placed in a covered Petri dish and allowed to fully dry out *via* solvent annealing. The substrates were then transferred to a glove box (MBraun) for post-annealing treatment on a hot plate at 120 °C for 10 min.

PEDOT:PSS (Orgacon EL-P 5015, Agfa) was screen printed on top of the IPA-pre-wetted P3HT:PCBM photoactive layer with a Presco flat-bed screen printer using mesh steel screens of different mesh sizes, to produce four different PEDOT:PSS layer thicknesses, namely 0.8 μm, 1.9 μm, 3.2 μm and 4.8 μm (indicated as HTL-08, HTL-19, HTL-32 and HTL-48 throughout the manuscript, respectively). The snap off distance and the printing speed in forward and backward directions for PEDOT:PSS screen printing were set at 1 mm and 2 mm/s, respectively. After printing, the samples were put into an oven at 120 °C to achieve a completely dry film. Before the deposition of the silver electrode, PSCs were transferred to a

nitrogen-filled glove box for heat treatment on a hotplate at 120 °C for 10 min.

To obtain the metallic back-electrode, the water-based reactive silver ink formulation was flexography-printed on top of the PEDOT:PSS layer using a Flexiproof 100 printer (RK PrintCoat Instruments Ltd.) with a ceramic anilox volume of 7 cm^3/m^2. The printing speed was set at 30 m/min. After deposition of the wet silver ink, the samples were placed in an oven and sintered for 15 min at 90 °C to obtain the complete PSC device. Reference PSC devices were also fabricated incorporating a 200-nm-thick silver electrode thermally evaporated in a nitrogen-filled glove box through a shadow mask. For all fabricated PSC devices, the active area was 0.32 cm^2. To test the scalability of the approach presented in this work, 1 cm^2 flexography-printed devices were also produced. At least six devices were fabricated and tested for each condition. A similar procedure was employed to obtain flexography-printed silver traces on PET substrates that were used to fully characterize the conductivity and the morphology of the flexography-printed conductive films.

2.3. Characterization

The current density–voltage (*J–V*) characteristics were recorded by illuminating the PSC devices with a solar simulator SolarTest 1200 (Atlas) set at 100 mW/cm^2, calibrated by means of a reference silicon PV cell equipped with a KG5 filter. The sheet resistance of silver and PEDOT:PSS layers was measured with a Keithley 2400 digital source-meter using the four-point probe method. The average thickness and surface roughness of the printed layers were measured using a Dektak 150 surface profiler (Veeco). Optical images of the silver electrodes were acquired using an Olympus BX-60 reflected-light optical microscope equipped with an Infinity 2 digital camera. A scanning electron microscope (SEM) (Carl Zeiss EVO 50 Extended Pressure, with an accelerating voltage of 15.00–17.50 kV) with integrated energy dispersive X-ray spectrometer (EDS) was used to investigate the diffusion of the reactive silver ink through the underlying PEDOT:PSS layer by means of cross-section SEM images and EDS analysis along the fractured surface of glass/ZnO/P3HT:PCBM/PEDOT:PSS/silver stacks.

3. Results and discussion

In order to investigate the possibility to obtain conductive traces by means of flexographic printing using the water-based silver precursor presented here, appropriate modification of the pristine silver ink formulation was required to make the ink flexographic printable. In particular, IPA was added to the ink formulation to enhance ink wetting on the ultimate target substrate (PEDOT:PSS). Furthermore, EP was used as a high-boiling-point diluent (T_b=132 °C) to reduce the evaporation rate of the solvent system after deposition of the ink thus allowing to obtain a homogenous surface morphology of the printed features. After a preliminary screening, an optimal 10 wt% diluent concentration (EP:IPA=70:30 wt/wt) in the formulation was used to ensure printability of the silver ink and at the same time to maintain a relatively high concentration of silver precursor in the reactive ink formulation. In addition to EP and IPA additives, PVP was also included in the ink formulation to serve as binder so as to promote improved adhesion of the ink onto the target substrate and also to adjust the rheological properties of the ink (see Supporting information). PVP was selected because of its high water solubility, considering the water-based nature of the reactive silver ink. Different concentrations of PVP were investigated in the 0.5–3 wt% range and their effect on the electrical properties of the flexographic printed silver traces of constant thickness (1.6 μm with mean surface roughness of 0.6 μm) was evaluated. The sheet resistance R_{sheet} of the printed silver traces was found to increase significantly after the addition of PVP to the silver ink formulation, indicating that the presence of the binder clearly affects the electrical conduction properties of the silver ink (see Supporting information). In particular, a one-order-of-magnitude R_{sheet} increase was observed upon addition of 0.5 wt% of PVP (R_{sheet} =7.2 Ω/sq) to the pristine silver ink (R_{sheet} =0.7 Ω/sq, as measured on 1.6 μm thick drop casted films). Furthermore, R_{sheet} was found to progressively increase at increasing PVP concentrations leading to non-conductive traces for PVP concentrations higher than 3 wt%. Following these preliminary tests, a PVP concentration of 0.5 wt% in the silver ink was therefore used in the fabrication of the PSC devices as it represents the minimum PVP concentration to ensure ink printability with a flexographic printer and simultaneously the maximum PVP concentration to minimize the R_{sheet} of the printed electrodes.

After optimization of the ink formulation to achieve conductive printed silver features, PSC devices with inverted structure were fabricated onto flexible substrates. In order to investigate the effect of the architecture of the back-electrode on the performance of the PSC devices, different flexography-printed back-electrode configurations were considered (Fig. 1c), namely full-coverage back electrode (F-FC), metallic grid with two fingers (F-G2F) and metallic grid with four fingers (F-G4F). The grid structure was composed by parallel fingers printed onto the active area inte-grated to a bus bar for the electrical contact required for current density–voltage (*J–V*) measurements. To evaluate the extent of the contribution of the metallic back electrode on device performance, PSC devices incorporating the sole screen-printed PEDOT:PSS layer as back electrode (without metallic silver ink) were also fabricated (S-PP).

Fig. 2a shows the *J–V* characteristics for devices incorporating a 0.8 μm thick PEDOT:PSS layer (HTL-08) and different back-electrode configurations (S-PP, F-G2F, F-G4F and F-FC). F-FC devices exhibit the poorest performance, with an open-circuit voltage V_{oc} of 0.20 V, a short-circuit current density J_{sc} of 1.97 mA/cm^2, a fill factor FF of 25.15% and a power conversion efficiency PCE of 0.10%. As opposed to this, the use of a metal grid (two or four fingers) results in improved electrical response, as evidenced by the increase in both V_{oc} and J_{sc} values registered in F-G2F (V_{oc}=0.45 V, J_{sc} =2.22 mA/cm^2) and F-G4F (V_{oc}=0.44 V, J_{sc}=2.35 mA/cm^2) devices as compared to F-FC systems. Such improved performance may be related to the better charge injection into the metallic electrode in the case of metal grids, likely ascribable to better interfacial contacts between silver metal grids and the underlying PEDOT:PSS layer as compared to the full-coverage configuration [33]. In particular, the presence of defects and inhomogeneous features is largely increased in the case of the full-coverage metallic electrode because of the larger printed area involved as opposed to metallic grids, thus significantly increasing the prob-ability of shunts in the device.

In addition, full-coverage electrodes may yield an increase in parasitic resistance within the PSC device due to physical damages of the underlying PEDOT:PSS layer resulting from the presence of a larger volume of deposited silver ink than in the case of metallic grids. Such negative interaction between silver ink and PEDOT:PSS may lead to penetration of the silver ink into the photoactive layer, thus resulting in the formation of contaminations and defects in the BHJ network that may be responsible for the drop in PV performance. As opposed to this, the metal grid electrode structure allows for a reduction of the volume of silver ink coming into contact with the PEDOT:PSS layer, leading to a lower amount of ink penetrating into the device stack and reaching the BHJ layer. A similar effect was recently highlighted on screen printed back-electrodes [24]. It is interesting to note that in the case of devices

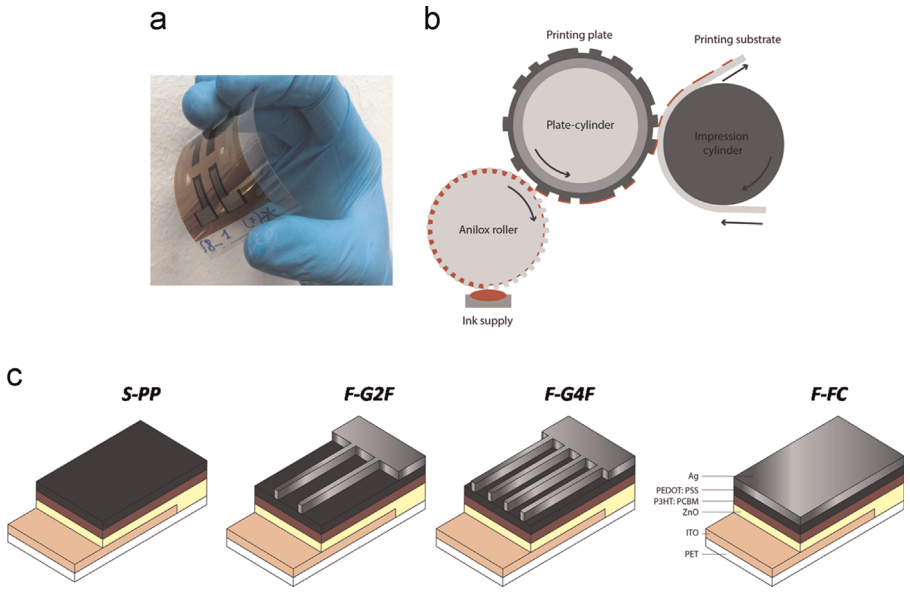

Fig. 1. (a) PSC devices produced on flexible substrate by all solution R2R-compatible processes; (b) schematic illustration of flexographic printing; (c) PSC layer stack and back electrode structures investigated in this work: PEDOT:PSS as electrode (S-PP), silver grid structure with two (F-G2F) and four (F-G4F) fingers and full-coverage silver layer (F-FC).

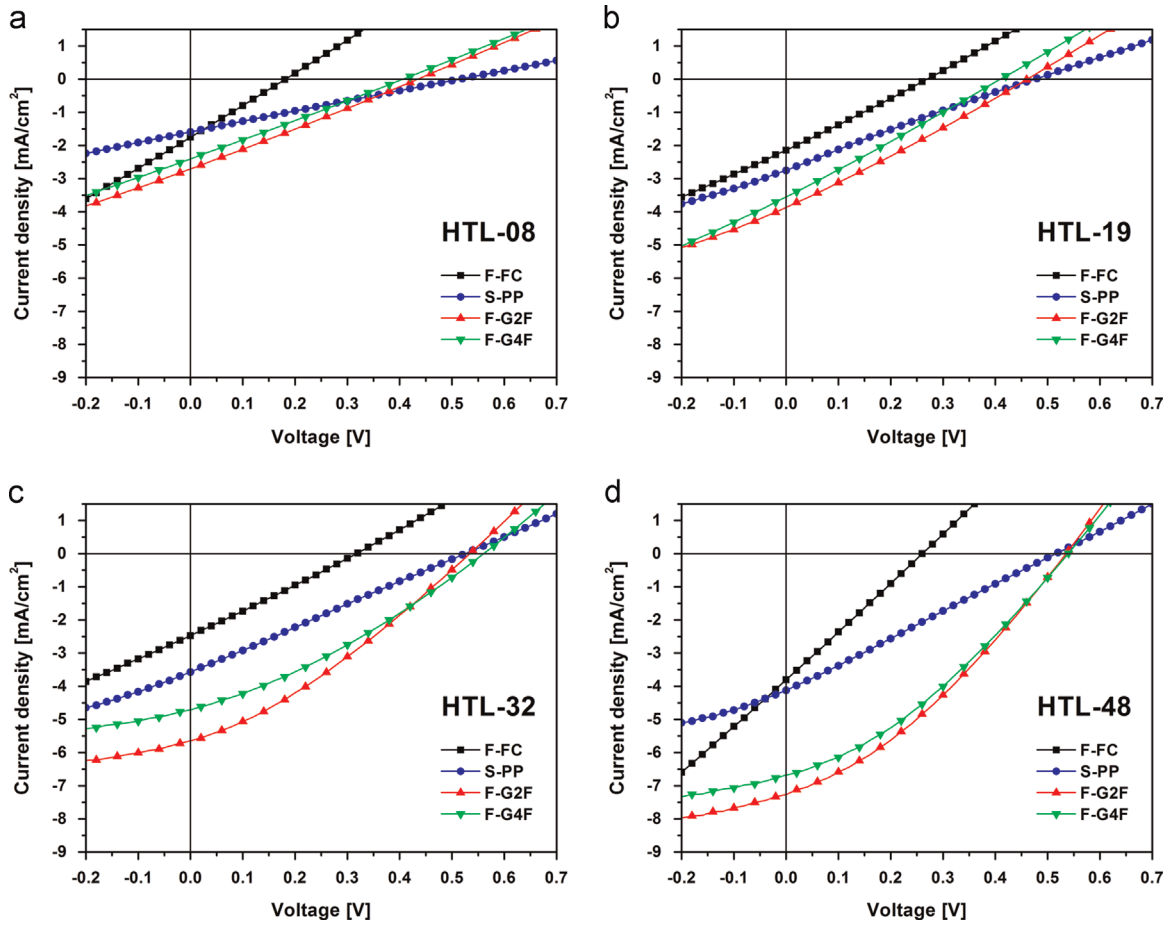

Fig. 2. *J–V* characteristics of PSC devices with different back-electrode architectures measured at different PEDOT:PSS thicknesses: (a) 0.8 μm (HTL-08), (b) 1.9 μm (HTL-19), (c) 3.2 μm (HTL-32) and (d) 4.8 μm (HTL-48).

incorporating only PEDOT:PSS as counter electrode (S-PP), lower efficiencies are observed compared to PSC devices with metal grid electrode structure (both F-G2F and F-G4F), clearly indicating that the use of the grid electrode based on the silver ink developed in this work is necessary to achieve efficient charge extraction and collection from the PSC devices.

Table 1
Effect of PEDOT:PSS thickness and back-electrode structure on the average photovoltaic parameters of the PSC devices studied in this work.

Sample	PEDOT:PSS Thickness [μm]	V_{oc} [V]	J_{sc} [mA/cm^2]	FF [%]	PCE [%]	R_s [Ω cm^2]	R_{sh} [Ω cm^2]
S-PP	0.8	0.51 ± 0.01	1.59 ± 0.50	22.60 ± 2.17	0.19 ± 0.07	266 ± 19	299 ± 22
F-FC	0.8	0.20 ± 0.03	1.97 ± 0.30	25.15 ± 0.03	0.10 ± 0.03	86 ± 11	78 ± 12
F-G2F	0.8	0.45 ± 0.04	2.22 ± 0.72	25.53 ± 0.38	0.27 ± 0.10	189 ± 23	246 ± 31
F-G4F	0.8	0.44 ± 0.05	2.35 ± 0.81	24.30 ± 2.69	0.26 ± 0.13	149 ± 21	183 ± 27
S-PP	1.9	0.49 ± 0.03	2.10 ± 1.02	22.26 ± 1.74	0.23 ± 0.13	192 ± 20	329 ± 34
F-FC	1.9	0.23 ± 0.06	1.99 ± 0.22	25.24 ± 0.51	0.12 ± 0.05	53 ± 7	93 ± 11
F-G2F	1.9	0.45 ± 0.03	3.85 ± 0.66	26.16 ± 0.38	0.46 ± 0.10	96 ± 14	280 ± 27
F-G4F	1.9	0.41 ± 0.05	3.07 ± 0.97	25.74 ± 0.32	0.34 ± 0.14	101 ± 13	207 ± 21
S-PP	3.2	0.53 ± 0.02	3.66 ± 0.92	24.24 ± 1.62	0.49 ± 0.10	119 ± 11	563 ± 27
F-FC	3.2	0.28 ± 0.05	3.18 ± 1.00	25.57 ± 0.44	0.22 ± 0.03	52 ± 8	86 ± 7
F-G2F	3.2	0.53 ± 0.02	5.20 ± 0.78	31.35 ± 3.04	0.92 ± 0.12	59 ± 6	1141 ± 96
F-G4F	3.2	0.52 ± 0.05	4.68 ± 0.96	31.30 ± 1.62	0.82 ± 0.16	66 ± 9	988 ± 85
S-PP	4.8	0.53 ± 0.01	4.44 ± 1.52	24.40 ± 2.37	0.55 ± 0.20	104 ± 8	1126 ± 98
F-FC	4.8	0.28 ± 0.02	3.70 ± 0.14	25.31 ± 0.05	0.26 ± 0.01	50 ± 6	62 ± 7
F-G2F	4.8	0.54 ± 0.02	7.03 ± 0.58	33.92 ± 1.28	1.26 ± 0.09	41 ± 2	1189 ± 58
F-G4F	4.8	0.52 ± 0.01	6.69 ± 0.73	33.80 ± 0.61	1.16 ± 0.18	45 ± 4	1073 ± 53

As shown in Fig. 2 and Table 1, the PV trends reported on HTL-08 devices related to the architecture of the counter electrode are observed also at different PEDOT:PSS thicknesses. More specifi-cally, PSC devices incorporating the metallic silver grid electrode are found to constantly outperform F-FC (full-coverage) as well as S-PP (PEDOT:PSS only) devices even for higher PEDOT:PSS thick-nesses, further demonstrating the beneficial effect of such elec-trode architecture on device performance. Moreover, no significant performance differences are observed between F-G2F (two-finger grid) and F-G4F (four-finger grid) electrodes, suggesting compar-able interfacial interactions between PEDOT:PSS and metal grid for these two configurations. The effect of PEDOT:PSS thickness on device performance can be clearly appreciated by considering the PV response of PSC devices with similar electrode architecture at increasing PEDOT:PSS thickness. As presented in Table 1, increas-ing the thickness of the HTL results in improved device perfor-mance for homologous electrode configurations. In particular, a visible increase of J_{sc} from 2.22 mA/cm^2 to 7.03 mA/cm^2 is observed with increasing PEDOT:PSS thickness from 0.8 μm to 4.8 μm in F-G2F systems. Similar results are found on F-G4F. In addition, F-G2F and F-G4F electrode configurations exhibit a well-defined improvement of the diode characteristics for PEDOT:PSS layer thicknesses above 3 μm, resulting from a clear improvement in the FF of the PSC device that is found to increase from about 25% to 34% for 0.8 μm and 4.8 μm thick PEDOT:PSS layers, respectively. Such an improvement may be correlated with the increase in shunt resistance (R_{sh}) observed with increasing PEDOT:PSS layer thickness, likely resulting from reduced ink diffusion towards the BHJ for thicker HTLs. In particular, as shown in Table 1 the value of R_{sh} is found to increase from 246 Ω cm^2 to 1189 Ω cm^2 for F-G2F-08 and F-G2F-48, respectively. Notably, defects and damages to the organic layer may cause the formation of leakage currents across the solar cell that in turn determine lower R_{sh} and FF values [34]. Moreover, leakage currents can also affect the V_{oc} of the PSC device [35] and may be partly responsible for the lower values of V_{oc} found in devices with PEDOT:PSS layer thicknesses below 2 μm. In addition to the increased R_{sh}, a decrease in series resistance (R_s) of PSC devices may also be responsible for the increase of FF at increasing PEDOT:PSS layer thicknesses. As shown in Table 1, R_s is found to decrease substantially in F-G2F devices from 189 Ω cm^2 to 41 Ω cm^2 for PEDOT:PSS thicknesses of 0.8 μm and 4.8 μm, respectively. A similar behavior is observed on F-G4F devices. This trend may be explained by considering that R_s is strongly related to the sheet resistance of the back electrode [35]. In this case, because the conductivity of the silver electrode is constant for all electrode configurations (the thickness of the metallic trace is constant), the variations in sheet resistance of the electrode can be largely attributed to the thickness of the PEDOT:PSS layer. In particular, the sheet resistance of the PEDOT:PSS layer was found to be inversely proportional to the layer thickness, with values of 186 Ω/sq, 89 Ω/sq, 63 Ω/sq and 32 Ω/sq for PEDOT:PSS thicknesses of 0.8 μm,1.9 μm, 3.2 μm and 4.8 μm, respectively (Supporting information). Accordingly, lower R_s values are obtained for PSC devices incorporating thicker HTLs. Additionally, the ohmic contact between the photoactive material and the metallic electrode is improved for increasing PEDOT:PSS thicknesses because of limited silver ink penetration towards the BHJ, ultimately leading to lower R_s and improved PV response. These results further confirm the essential role played by the PEDOT:PSS layer in preventing shunting effects and damages to the BHJ layer caused by silver ink diffusion through the HTL and ultimately in achieving optimal PV performance. To evaluate the potential scalability of the silver ink formulation developed in this work, larger area (1 cm^2) PSC devices were also fabricated incorporating flexo-graphy-printed multi-finger grid silver electrodes (Supporting information). To take into account the effect of PEDOT:PSS thick-ness on device performance, a 4.8 μm thick PEDOT:PSS layer was employed to limit the potential degradation of the BHJ material. As compared to 0.32 cm^2 devices, a slight decrease of device effi-ciency was observed for larger area PSCs originating from a decrease in J_{sc} and FF. These trends are in agreement with litera-ture reports and can be correlated with the increased electrical resistive losses associated with the increased device active area [36–39].

To evaluate the performance of the newly proposed flexo-graphy-printed silver electrode, reference PSC devices incorpor-ating the metallic electrode with grid configuration (both two fingers – E-G2F and four fingers – E-G4F) deposited *via* thermal evaporation were also produced and the results of the PV char-acterization are presented in Table 2. A slight increase in PCE is observed in E-G4F devices compared with E-G2F devices, mainly resulting from improved J_{sc} and FF. In addition, no significant performance improvements are observed by increasing the PEDOT:PSS layer thickness. These results may be explained by considering that the thermal evaporation technique allows to achieve a very smooth and homogeneous metallic electrode without physically damaging the underlying polymeric layer. In addition, no solvent is present during thermal evaporation of the silver electrode, thus chemical degradation of the PEDOT:PSS and BHJ layers is prevented. As a result, a larger electrode area (four-

Table 2
Average photovoltaic parameters of reference PSC devices incorporating different evaporated silver metal grid electrode configurations.

Sample	PEDOT:PSS Thickness [μm]	V_{oc} [V]	J_{sc} [mA/cm^2]	FF [%]	PCE [%]	R_s [Ω cm^2]	R_{sh} [Ω cm^2]
E-G2F	0.8	0.52 ± 0.01	5.67 ± 0.44	28.52 ± 0.87	0.85 ± 0.05	65 ± 6	965 ± 18
E-G4F	0.8	0.52 ± 0.01	6.80 ± 0.34	37.01 ± 0.15	1.32 ± 0.08	35 ± 4	1196 ± 46
E-G2F	1.9	0.51 ± 0.01	6.20 ± 0.26	30.46 ± 2.03	0.96 ± 0.08	52 ± 6	997 ± 6
E-G4F	1.9	0.50 ± 0.01	6.73 ± 0.02	35.42 ± 2.80	1.20 ± 0.06	31 ± 2	1227 ± 36
E-G2F	3.2	0.53 ± 0.01	5.96 ± 0.51	34.45 ± 1.06	1.09 ± 0.05	43 ± 3	986 ± 24
E-G4F	3.2	0.53 ± 0.01	6.35 ± 0.10	38.49 ± 0.16	1.30 ± 0.02	30 ± 4	1227 ± 31
E-G2F	4.8	0.45 ± 0.02	6.79 ± 1.41	30.01 ± 1.72	0.92 ± 0.19	30 ± 5	981 ± 38
E-G4F	4.8	0.50 ± 0.01	7.41 ± 1.66	33.87 ± 0.40	1.25 ± 0.25	27 ± 3	1098 ± 31

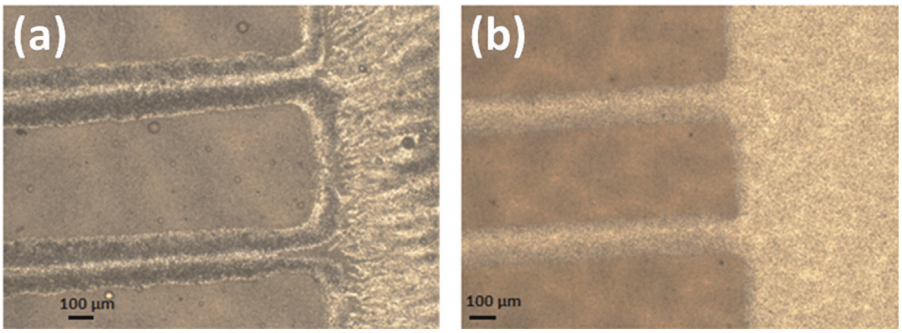

Fig. 3. Optical microscope images of (a) flexography-printed and (b) thermally evaporated silver grid electrodes.

finger as opposed to two-finger metallic grid) in reference evaporated devices only results in improved ohmic contact and better charge extraction, in turn leading to improved PV response. It is worth highlighting that the performance obtained with optimized devices incorporating the flexography-printed reactive silver ink as counter electrode with grid configuration is comparable with that registered in devices with thermally evaporated silver grid, clearly indicating the potential of the newly proposed low-annealing-temperature silver ink as precursor for solution-pro-cessable silver electrodes in inverted PSC devices entirely fabri-cated in air.

In order to better elucidate the trends observed on device behavior, a morphological analysis was conducted on the silver grid electrodes fabricated *via* flexographic printing and thermal evaporation. To this end, optical microscope images of both flexography-printed and thermally evaporated silver grids were recorded and the results of the analysis are shown in Fig. 3. Both the printing plate used for flexographic printing and the shadow mask used for thermal evaporation of the silver grid were designed to give a nominal finger width of 100 μm. However, as shown in Fig. 3a, flexography-printed silver electrodes show a finger width of about 200 μm (Fig. 3a) as compared to thermally evaporated silver electrodes in which a finger width of 100 μm is observed (Fig. 3b). Such discrepancy can be attributed to the ink spread commonly observed in flexographic printing due to the nip pressure acting on the target substrate (PEDOT:PSS) and to the flexible printing plate, leading in this case to a larger active surface coverage as compared to that obtained with evaporated grids. Nominal coverage percentages of 3.75% and 7.5% were calculated for the two-finger and four-finger grid electrode configurations, respectively, by computing the ratio between the area covered by the multi-finger grid overlapping the PSC device active area and the entire active area of the PSC device. While in the case of devices incorporating the thermally evaporated grid electrode the actual coverage is found to match the nominal values, the flexography printed grid electrodes exhibit a two-fold increase in sur-face coverage, with values of 7.5% and 15% for grid electrodes with two and four fingers, respectively. Such behavior may be correlated with the PV results presented in Tables 1 and 2, where PSC devices incorporating a flexography-printed silver electrode with a two-finger configuration were found to give comparable performance to that obtained from PSC devices with thermally-evaporated four-finger grid electrodes. In addition to the ink spread, the optical images of the flexography-printed grid electrode also show two characteristic features of flexographic printing technology that affect the surface morphology of the printed feature. Firstly, the viscous fingering instability, parallel to the printing direction, can be easily identified in the bus bar section. This printing characteristic originates from the ink splitting between the printing plate and the target substrate [40]. Secondly, accumulation of ink is clearly visible along the edges of the printed fingers [41].

In the attempt to investigate the potential diffusion of the reactive silver ink through the PEDOT:PSS layer, model stack samples were produced with the configuration glass/ZnO/P3HT:PCBM/PEDOT:PSS/silver and fractured cross-sectional SEM images together with EDS analysis were recorded along the fractured surface at varying PEDOT:PSS layer thicknesses (Fig. 3). Since the main focus was on the interaction between the reactive silver ink and the PEDOT:PSS layer, a rigid substrate (glass) was used in this case so as to guarantee easier and more accurate sample preparation for the SEM analysis during the fracture cutting procedure (namely, a sharper fracture surface) compared to what was achievable with flexible devices. In addition, both the ZnO buffer layer and the photoactive layer were spin coated so as to reproduce the same thicknesses as those measured in the actual tested PSC devices. The PEDOT:PSS layer was screen printed using the same mesh screens used for device production and two different PEDOT:PSS layer thicknesses were investigated, namely 0.8 μm and 3.2 μm. Finally, the reactive silver ink was deposited on top of the stack as multi-finger grid structure with thickness of about 1.5 μm. As clearly shown in Fig. 4a, a thinner PEDOT:PSS layer allows significant reactive silver ink diffusion through the HTL, with the formation of silver channels that are found to fully penetrate the PEDOT:PSS layer and reach the underlying BHJ layer. This behavior leads to the generation of electrical shorts and to the

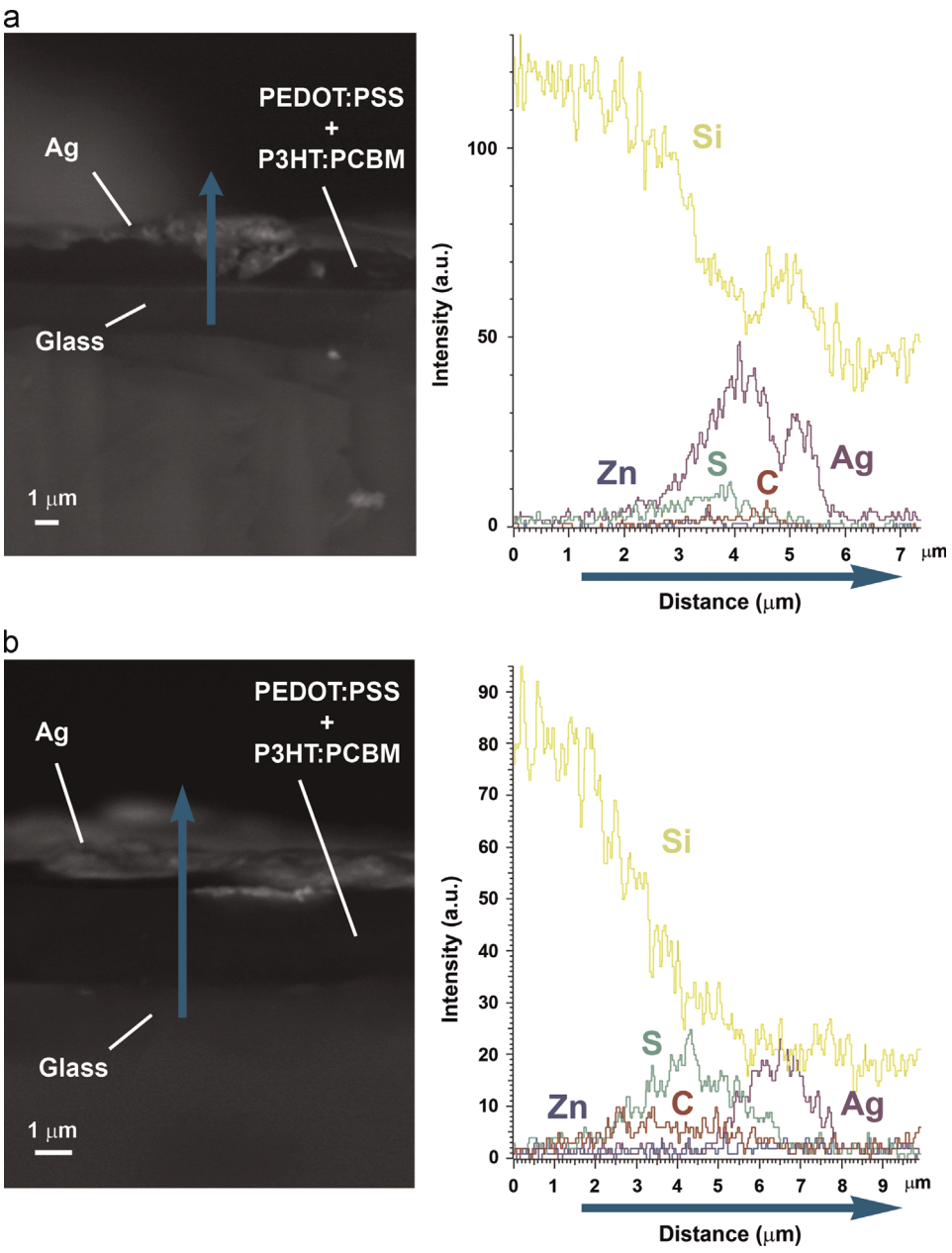

Fig. 4. Cross-sectional SEM images and corresponding EDS analysis along the cross-sectional area of fractured glass/ZnO/P3HT:PCBM/PEDOT:PSS/silver sample stack. Two different PEDOT:PSS layer thicknesses were investigated: (a) 0.8 μm and (b) 3.2 μm.

chemical degradation of the photoactive layer, in turn resulting in a reduction of photovoltaic performance, as observed from PV characterization of the PSC devices (Fig. 2 and Table 1). As opposed to this, thicker PEDOT:PSS layers are able to prevent such silver ink diffusion (Fig. 4b), thus allowing for improved device performance. These trends are further confirmed by the EDS measurements presented in Fig. 4, where the chemical composition of the multilayer stack along the cross-sectional surface is reported for the samples at different PEDOT:PSS layer thickness. Clearly, in the case of the stack incorporating the thinner PEDOT:PSS layer, the signal attributed to elemental silver is found almost along the entire cross-section, significantly overlapping with the carbon and sulfur signals that are associated with the presence of the underlying organic materials (PEDOT:PSS and P3HT:PCBM). On the other hand, only limited overlapping between the silver and the carbon and sulfur signals is found for thicker PEDOT:PSS layers (Fig. 4b), further demonstrating the critical role played by the thickness of the HTL in the limitation of the reactive silver ink diffusion through the sample stack towards the photoactive layer.

The presence of a silver grid electrode may allow for the potential use of PSC devices in double-side illumination applications, due to the semitransparency of the system. To this purpose, the PV behavior of PSC devices incorporating a flexography-printed two-finger grid electrode was evaluated upon back-side illumination (incident light coming from the silver grid side) at increasing PEDOT:PSS thickness. In particular, the PV parameters of these devices were recorded upon back-side illumination and normalized with respect to the corresponding values obtained from standard front-side illumination (incident light coming from the transparent PET substrate). The results are presented in Fig. 5, where J_{sc} and PCE trends are reported (no significant variations were observed on FF and V_{oc}).

As shown in Fig. 5, a progressive decrease of normalized PCE and J_{sc} is reported with increasing PEDOT:PSS layer thickness. In

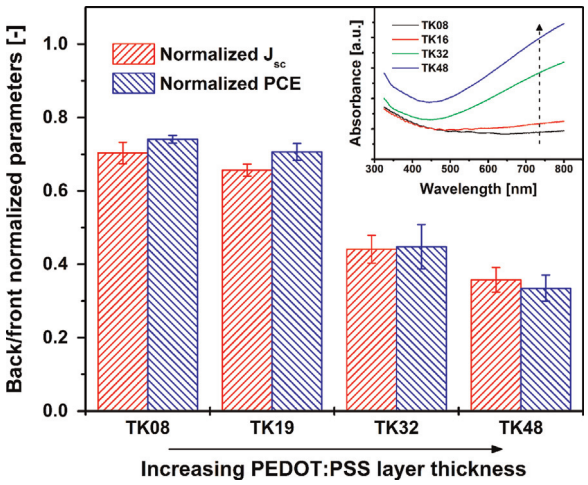

Fig. 5. PCE and J_{sc} of PSC devices (F-G2F) recorded upon back-side illumination for increasing PEDOT:PSS thicknesses. Values are normalized with respect to those obtained from front-side illumination. The inset shows the UV–vis spectra of PEDOT:PSS of increasing layer thicknesses (indicated by the dashed arrow).

particular, while in devices incorporating the thinnest PEDOT:PSS layer (F-G2F-08) back-side illumination allows one to preserve approximately 70% of the performance achievable with conventional front-side illumination, this ratio drops down to 35% for devices with the thickest PEDOT:PSS layer (F-G2F-48). This trend can be clearly correlated with the decrease in transmittance observed in the PEDOT:PSS layer by increasing its thickness (Fig. 5, inset). In the case of back-side illumination, a lower PEDOT:PSS transmittance determines a lower amount of photons being able to reach the photoactive layer, thus yielding a lower generated photocurrent and lower PCE for thicker layers. Since the configuration of the electrode is common to all PSC devices investigated in this case, the shading effect resulting from the presence of the silver grid on top of the PEDOT:PSS and BHJ layers (that inevitably determines a decrease in J_{sc} during back-side illumination) is not expected to alter significantly the observed trends.

4. Conclusion

In this work, a water-based solution-processable silver ink formulation with low annealing temperature was successfully employed as precursor for the fabrication of the metallic back-electrode in flexible inverted PSC devices produced by means of R2R-compatible printing techniques. Different back-electrode configurations were investigated and characterized to evaluate the effect of the deposition of such reactive silver ink on the underlying PSC layers. In addition, the influence of the thickness of the PEDOT:PSS buffer layer on the functional performance and morphology of the PSC devices was also investigated. It was found that, for the same PEDOT:PSS thickness, devices incorporating a silver electrode with multi-finger grid structure outperformed those equipped with a full-coverage electrode configuration. As evidenced from morphological analysis of the vertical multilayered PSC stack, this effect was correlated with the amount of silver ink that can penetrate through the PEDOT:PSS layer into the underlying PSC layers and cause shunting effects, the latter being significantly higher in the case of full-coverage electrode configuration as opposed to the multi-finger grid structure. To this end, it was observed that the thickness of the PEDOT:PSS layer represents a crucial parameter in order to ensure correct functioning of the PSC devices. In particular, an optimized combination of back-electrode architecture and PEDOT:PSS thickness was found, that also allowed to obtain functioning semi-transparent PSC devices. In conclusion, the results of this study demonstrate a viable and straightforward route to obtain metallic back-electrodes for flexible inverted PSC devices starting from a solution-processable water-based reactive silver ink formulation with low-annealing temperature, and provide useful insights into the key role played by electrode geometry and PEDOT:PSS buffer layer in the fabrication of fully functional R2R-compatible flexible PSC devices. Further work will be focused on the optimization of the silver ink formulation and its chemical compatibility with the underlying PEDOT:PSS buffer layer. In particular, alternative milder diluents will be sought for the silver precursor so as to enable its successful deposition also onto thin PEDOT:PSS layers without detrimental effects on the BHJ, ultimately allowing for optimized device performance.

Appendix A. Supplementary material

Supplementary data associated with this article can be found in the online version.

References

[1] F.C. Krebs, T. Tromholt, M. Jørgensen, Upscaling of polymer solar cell fabrication using full roll-to-roll processing, Nanoscale 2 (2010) 873–886.
[2] R.R. Søndergaard, M. Hösel, F.C. Krebs, Roll-to-roll fabrication of large area functional organic materials, J. Polym. Sci. Part B: Polym. Phys. 51 (2013) 16–34.
[3] F.C. Krebs, All solution roll-to-roll processed polymer solar cells free from indium–tin-oxide and vacuum coating steps, Org. Electron. 10 (2009) 761–768.
[4] C.-C. Chen, L. Dou, R. Zhu, C.-H. Chung, T.-B. Song, Y.B. Zheng, S. Hawks, G. Li, P.S. Weiss, Y. Yang, Visibly transparent polymer solar cells produced by solution processing, ACS Nano 6 (2012) 7185–7190.
[5] H.-Y. Chen, J. Hou, S. Zhang, Y. Liang, G. Yang, Y. Yang, Polymer solar cells with enhanced open-circuit voltage and efficiency, Nat. Photonics 3 (2009) 649–653.
[6] Y. Sun, G.C. Welch, W.L. Leong, C.J. Takacs, G.C. Bazan, Solution-processed small-molecule solar cells with 6.7% efficiency, Nat. Mater. 11 (2012) 44–48.
[7] C. Cui, W.-Y. Wong, Y. Li, Improvement of open-circuit voltage and photovoltaic properties of 2D-conjugated polymers by alkylthio substitution, Energy Environ. Sci. 7 (2014) 2276–2284.
[8] S. Woo, W.H. Kim, H. Kim, Y. Yi, H.-K. Lyu, Y. Kim, 8.9% Single-stack inverted polymer solar cells with electron-rich polymer nanolayer-modified inorganic electron-collecting buffer layers, Adv. Energy Mater. 4 (2014) 1301692–1301699.
[9] J.D. Douglas, G. Griffini, T.W. Holcombe, E.P. Young, O.P. Lee, M.S. Chen, J.M.J. Fréchet, Functionalized isothianaphthene monomers that promote quinoidal character in donor-acceptor copolymers for organic photovoltaics, Macromolecules 45 (2012) 4069–4074.
[10] C.-C. Chen, W.-H. Chang, K. Yoshimura, K. Ohya, J. You, J. Gao, Z. Hong, Y. Yang, An efficient triple-junction polymer solar cell having a power conversion efficiency exceeding 11%, Adv. Mater. 26 (2014) 5670–5677.
[11] A. Rivaton, A. Tournebize, J. Gaume, P.-O. Bussière, J.-L. Gardette, S. Therias, Photostability of organic materials used in polymer solar cells, Polym. Int. 63 (2014) 1335–1345.
[12] G. Griffini, S. Turri, M. Levi, Degradation and stabilization of poly(3-hexylthiophene) thin films for photovoltaic applications, Polym. Bull. 66 (2011) 211–222.
[13] G. Griffini, J.D. Douglas, C. Piliego, T.W. Holcombe, S. Turri, J.M.J. Fréchet, J.L. Mynar, Long-term thermal stability of high-efficiency polymer solar cells based on photocrosslinkable donor-acceptor conjugated polymers, Adv. Mater. 23 (2011) 1660–1664.
[14] M. Jørgensen, K. Norrman, S.A. Gevorgyan, T. Tromholt, B. Andreasen, F.C. Krebs, Stability of polymer solar cells, Adv. Mater. 24 (2012) 580–612.
[15] F.C. Krebs, K. Norrman, Analysis of the failure mechanism for a stable organic photovoltaic during 10,000 h of testing, Prog. Photovolt.: Res. Appl. 15 (2007) 697–712.
[16] F.C. Krebs, R. Søndergaard, M. Jørgensen, Printed metal back electrodes for R2R fabricated polymer solar cells studied using the LBIC technique, Sol. Energy Mater. Sol. Cells 95 (2011) 1348–1353.
[17] F. Zhang, X. Xu, W. Tang, J. Zhang, Z. Zhuo, J. Wang, J. Wang, Z. Xu, Y. Wang, Recent development of the inverted configuration organic solar cells, Sol. Energy Mater. Sol. Cells 95 (2011) 1785–1799.
[18] C.-H. Hsieh, Y.-J. Cheng, P.-J. Li, C.-H. Chen, M. Dubosc, R.-M. Liang, C.-S. Hsu, Highly efficient and stable inverted polymer solar cells integrated with a

cross-linked fullerene material as an interlayer, J. Am. Chem. Soc. 132 (2010) 4887–4893.
[19] Y. Sahin, S. Alem, R. de Bettignies, J.-M. Nunzi, Development of air stable polymer solar cells using an inverted gold on top anode structure, Thin Solid Films 476 (2005) 340–343.
[20] M. Hösel, R.R. Søndergaard, D. Angmo, F.C. Krebs, Comparison of fast roll-to-roll flexographic, inkjet, flatbed, and rotary screen printing of metal back electrodes for polymer solar cells, Adv. Energy Mater. 15 (2013) 995–1001.
[21] C. Girotto, B.P. Rand, S. Steudel, J. Genoe, P. Heremans, Nanoparticle-based, spray-coated silver top contacts for efficient polymer solar cells, Org. Electron. 10 (2009) 735–740.
[22] J. Krantz, T. Stubhan, M. Richter, S. Spallek, I. Litzov, G.J. Matt, E. Spiecker, C.J. Brabec, Spray-coated silver nanowires as top electrode layer in semi-transparent P3HT:PCBM-based organic solar cell devices, Adv. Funct. Mater. 23 (2013) 1711–1717.
[23] S.K. Hau, H.-L. Yip, K. Leong, A.K.-Y. Jen, Spray coating of silver nanoparticle electrodes for inverted polymer solar cells, Org. Electron. 10 (2009) 719–723.
[24] D. Angmo, J. Sweelssen, R. Andriessen, Y. Galagan, F.C. Krebs, Inkjet printing of back electrodes for inverted polymer solar cells, Adv. Energy Mater. 3 (2013) 1230–1237.
[25] Y. Galagan, S. Shanmugam, J.P. Teunissen, T.M. Eggenhuisen, A.F.K. V. Biezemans, T. Van Gijseghem, W.A. Groen, R. Andriessen, Solution processing of back electrodes for organic solar cells, Sol. Energy Mater. Sol. Cells 130 (2014) 163–169.
[26] L. Blankenburg, K. Schultheis, H. Schache, S. Sensfuss, M. Schrödner, Reel-to-reel wet coating as an efficient up-scaling technique for the production of bulk-heterojunction polymer solar cells, Sol. Energy Mater. Sol. Cells 93 (2009) 476–483.
[27] H.J. Park, M.-G. Kang, S.H. Ahn, L.J. Guo, A facile route to polymer solar cells with optimum morphology readily applicable to a roll-to-roll process without sacrificing high device performance, Adv. Mater. 22 (2010) E247–E253.
[28] T. Kuwabara, T. Nakashima, T. Yamaguchi, K. Takahashi, Flexible inverted polymer solar cells on polyethylene terephthalate substrate containing zinc oxide electron-collection-layer prepared by novel sol–gel method and low-temperature treatments, Org. Electron. 13 (2012) 1136–1140.
[29] N. Espinosa, R. Garcia-Valverde, A. Urbina, F. Lenzmann, M. Manceau, D. Angmo, F.C. Krebs, Life cycle assessment of ITO-free flexible polymer solar cells prepared by roll-to-roll coating and printing, Sol. Energy Mater. Sol. Cells 97 (2013) 3–13.
[30] S.B. Walker, J.A. Lewis, Reactive silver inks for patterning high-conductivity features at mild temperatures, J. Am. Chem. Soc., 134, (2012) 1419–1421.
[31] M. Vilkman, P. Apilo, M. Välimäki, M. Ylikunnari, A. Bernardi, R. Po, G. Corso, J. Hast, Gravure-printed ZNO in fully roll-to-roll printed inverted organic solar cells: optimization of adhesion and performance, Energy Technol. 3 (2015) 407–413.
[32] M. Välimäki, P. Apilo, R. Po, E. Jansson, A. Bernardi, M. Ylikunnari, M. Vilkman, G. Corso, J. Puustinen, J. Tuominen, J. Hast, R2R-printed inverted OPV modules – towards arbitrary patterned designs, Nanoscale (2015), http://dx.doi.org/10.1039/C5NR00204D.
[33] B. de Boer, A. Hadipour, M.M. Mandoc, T. van Woudenbergh, P.W.M. Blom, Tuning of metal work functions with self-assembled monolayers, Adv. Mater. 17 (2005) 621–625.
[34] J. Weicker, H. Sun, C. Palumbiny, H.C. Hesse, L. Schmidt-Mende, Spray-deposited PEDOT:PSS for inverted organic solar cells, Sol. Energy Mater. Sol. Cells 94 (2010) 2371–2374.
[35] A. Moliton, J.M. Nunzi, Review how to model the behaviour of organic photovoltaic cells, Polym. Int. 55 (2006) 583–600.
[36] D. Gupta, M. Bag, K.S. Narayan, Area dependent efficiency of organic solar cells, Appl. Phys. Lett. 93 (2008) 163301.
[37] A.J. Das, K.S. Narayan, Retention of power conversion efficiency – from small area to large area polymer solar cells, Adv. Mater. 25 (2013) 2193–2199.
[38] J.D. Servaites, S. Yeganeh, T.J. Marks, M.A. Ratner, Efficiency enhancement in organic photovoltaic cells: consequences of optimizing series resistance, Adv. Funct. Mater. 20 (2010) 97–104.
[39] S. Choi, W.J. Potscavage Jr., B. Kippelen, Area-scaling of organic solar cells, J. Appl. Phys. 106 (2009) 054507.
[40] M. Hösel, F.C. Krebs, Large-scale roll-to-roll photonic sintering of flexo printed silver nanoparticle electrodes, J. Mater. Chem. 22 (2012) 15683–15688.
[41] H. Kipphan, Handbook of Print Media: Technologies and Production Methods, Springer-Verlag, Berlin Heidelberg, 2001.